XLVI CILAMCE
VITÓRIA - ES - BRAZIL - 2025
XLVI IBERO-LATIN AMERICAN CONGRESS ON COMPUTATIONAL METHODS IN ENGENEERING

A DEM-Based Simulation Framework for 3D Concrete Printing with the Discrete Fresh Concrete Model

Victor Hugo M. Avancini[1], Osvaldo D. Quintana-Ruiz[2], Eduardo M. B. Campello[1]

[1]*Dept. of Structural and Geotechnical Engineering, Polytechnic School, University of São Paulo, Brazil*
P.O. Box 61548, 05424-970, SP/São Paulo, Brazil
victor.avancini@usp.br, campello@usp.br
[2]*Computational Mechanics Laboratory, Faculty of Engineering, National University of Asunción, Campus de la UNA, San Lorenzo, Paraguay*
oquintana@ing.una.py

Abstract. Three-dimensional concrete printing (3DCP) is gaining traction as an innovative construction technique, offering notable advantages over conventional building methods. However, optimizing the material deposition process remains a key challenge, particularly concerning filament formation and stability during extrusion. This study combines the Discrete Element Method (DEM) with the Discrete Fresh Concrete (DFC) model to simulate the rheological behavior of fresh concrete during the printing process. We simulate two representative single-layer depositions — a circular path and a rectangular path — to assess the model's ability to reproduce realistic filament shapes under different geometric constraints. The results demonstrate the feasibility of using the DEM–DFC approach for capturing filament behavior during extrusion and for supporting future developments in 3D concrete printing simulations.

Keywords: 3D concrete printing, discrete element methods (DEM), discrete fresh concrete (DFC)

1 Introduction

Three-dimensional concrete printing (3DCP) has gained increasing attention in recent years as a novel construction technology that combines additive manufacturing with traditional civil engineering materials. By enabling automated, layer-by-layer deposition of concrete, 3DCP offers several advantages over conventional methods, including reduced material waste, lower labor costs, accelerated construction timelines, and greater design freedom [1, 2]. Furthermore, it facilitates the use of sustainable materials such as geopolymers and earth-based mixes, contributing to more eco-efficient building practices.

Despite its potential, widespread implementation of 3DCP faces several technical challenges, particularly concerning the rheological behavior of fresh concrete during pumping, extrusion, and deposition. Key issues include the control of filament shape, stability, and inter layer bonding, all of which are influenced by the properties of the concrete mixture and process parameters such as printing speed and nozzle design [2, 3].

To address these challenges, numerical modeling has emerged as a powerful tool to support the development and optimization of 3DCP. Among the available techniques, the Discrete Element Method (DEM) [4–6] is particularly suitable for simulating fresh concrete, as it naturally accounts for the discrete character of the material at the aggregate scale. The DEM enables the modeling of individual particles and their interactions based on mechanical contact laws, offering insights into particle trajectories, velocities, and contact forces that are difficult to obtain experimentally [7].

In the context of fresh concrete, several efforts have been made to extend DEM for rheological modeling, including the development of the Discrete Fresh Concrete (DFC) model by Cusatis and Ramyar [8]. The DFC model introduces a two-phase particle representation, in which each aggregate is surrounded by a soft mortar layer, allowing for the simulation of both elastic and viscous behavior of the composite system. However, limitations remain in accurately capturing tangential energy dissipation, particularly during directional processes such as filament deposition.

In a previous work [9], such limitations were addressed through the incorporation of static friction and rolling resistance into the DFC model. Although these improvements are not explored in the present study, they form the foundation for future developments of the present simulation framework.

In this work, we implement the DFC model within an in-house DEM formulation (see our early developments in [10]) to simulate 3D concrete printing. We simulate two representative single-layer depositions – a circular path and a rectangular path — to assess the model's ability to reproduce realistic filament shapes under different geometric constraints. The results demonstrate the feasibility of using the DEM–DFC approach for capturing filament behavior during extrusion, and for supporting future developments in 3D concrete printing simulations.

2 Methodology

2.1 Particle dynamics

The dynamics of each particle are governed by a Lagrangian formulation of the Discrete Element Method (DEM), where particle are idealized as rigid spheres characterized by mass m_i, radius R_i, and rotation inertia $j_i = \frac{2}{5} m_i R_i^2$. The motion equations for translation and rotation follow the classical Newton-Euler formalism:

$$m_i \dot{\boldsymbol{v}}_i = \boldsymbol{f}_i^{con} + \boldsymbol{f}_i^{env}, \qquad j_i \dot{\boldsymbol{\omega}}_i = \boldsymbol{m}_i^{fric} + \boldsymbol{m}_i^{rol}, \tag{1}$$

where $\boldsymbol{f}_i^{con}$ are the forces due to mechanical contacts with other particles or objects (which include both normal and tangential/frictional components), $\boldsymbol{f}_i^{env}$ are the forces due to the environment, $\boldsymbol{m}_i^{fric}$ are the moments induced by the frictional components of the contact forces, and $\boldsymbol{m}_i^{rol}$ are the moments induced by rolling resistance effects. In this study, the environment force is limited to gravity: $\boldsymbol{f}_i^{env} = m_i \boldsymbol{g}$.

The total contact force acting on particle i results from the sum of all pairwise interactions with its neighboring contacts:

$$\boldsymbol{f}_i^{con} = \sum_{j=1}^{N_c^i} (\boldsymbol{f}_{ij}^{con,n} + \boldsymbol{f}_{ij}^{con,t}), \tag{2}$$

where $\boldsymbol{f}_{ij}^{con,n}$ and $\boldsymbol{f}_{ij}^{con,t}$ are the normal and tangential components, respectively, of the force acting on particle i due to its contact with particle (or object) j, and N_i^c is the number of particles and objects in contact with particle i.

The normal contact force $\boldsymbol{f}_{ij}^{con,n}$ follows Hertz contact theory, given by

$$\boldsymbol{f}_{ij}^{con,n} = -\frac{4}{3} \sqrt{R^*} E^* \delta_{ij}^{3/2} \boldsymbol{n}_{ij} - d^n \dot{\delta}_{ij} \boldsymbol{n}_{ij} \tag{3}$$

where δ_{ij} is the overlap between particles i and j:

$$\delta_{ij} = ||\boldsymbol{x}_i - \boldsymbol{x}_j|| - R_i + R_j, \tag{4}$$

and $\dot{\delta}_{ij}$ is the overlap velocity. The unit vector $\boldsymbol{n}_{ij}$ points from the center of particle i to j, given by

$$\boldsymbol{n}_{ij} = \frac{\boldsymbol{x}_j - \boldsymbol{x}_i}{||\boldsymbol{x}_j - \boldsymbol{x}_i||}. \tag{5}$$

The effective radius R^*, effective elastic modulus E^* and effective mass m^* are given by

$$R^* = \frac{R_i R_j}{R_i + R_j}, \qquad E^* = \frac{E_i E_j}{E_j(1-\nu_i^2) + E_i(1-\nu_j^2)} \qquad \text{and} \qquad m^* = \frac{m_i m_j}{m_i + m_j}. \tag{6}$$

The contact damping constant d^n, representing viscous energy dissipation in the contact normal direction, is given by

$$d^n = 2\xi^n \sqrt{2E^* m^* \sqrt{R^*}} \delta_{ij}^{1/4}, \tag{7}$$

where ξ^n is the contact damping rate.

The tangential contact force $\boldsymbol{f}_{ij}^{con,t}$ depends on the relative tangential displacement $\Delta \boldsymbol{x}_{ij}$ at the contact interface. Following the Coulomb model, we compute it though trials — denoted as $\boldsymbol{f}_{ij}^{con,t,trial}$, with a trial relative tangential displacement $\Delta \boldsymbol{x}_{ij}^{trial}$ —, using a spring-dashpot model, given by

$$\boldsymbol{f}_{ij}^{con,t} = -(k^t \Delta \boldsymbol{x}_{ij} + d^t \boldsymbol{v}_{ij}) \tag{8}$$

where $\Delta \boldsymbol{x}_{ij}$ is the accumulated relative tangential displacement and $\boldsymbol{v}_{ij}$ is the relative tangential velocity between i and j at their contact point. The tangential stiffness between i and j (obtained from Mindlin's elastic solution for sticking spheres, see, e.g., Johnson [11]) is given by

$$k^t = 8G^*\sqrt{R^*}|\delta_{ij}|^{1/2} \qquad \text{with} \qquad G^* = \frac{G_i G_j}{2G_i + 2G_j - G_i\nu_j - G_j\nu_i}, \tag{9}$$

while d^t is the damping constant of the tangential force, given by

$$d^t = 2\xi^t\sqrt{m^* k^t}, \tag{10}$$

where ξ^t is the tangential damping ratio. The relative tangential displacement is computed incrementally by integrating the relative tangential velocity $\boldsymbol{v}_{ij}$ between particles i and j at their contact point. If the resulting tangential contact force exceeds the static friction limit, dynamic friction is applied instead, depending on the static and dynamic friction coefficients of the contacting pair (see Campello [12]).

Due to the eccentricity of the tangential forces relative to particle centers, moments are induced and given by

$$\boldsymbol{m}_i^{fric} = \sum_{j=1}^{N_i^c} \boldsymbol{r}_i^P \times \boldsymbol{f}_{ij}^{con,t} \tag{11}$$

where $\boldsymbol{r}_i^P$ is the vector from the center of particle i to the contact point P with particle j.

In additional, the rolling resistance moment is an effect of the deformation that a particle undergoes when it rolls over another particle (or object). The resulting rolling resistance moment acting on a particle i, due to rolling interactions with N_i^c other particles (or objects), is given by

$$\boldsymbol{m}_i^{rol} = \sum_{j=1}^{N_i^c} \boldsymbol{m}_{ij}^{rol}, \tag{12}$$

where $\boldsymbol{m}_{ij}^{rol}$ is the rolling resistance moment on particle i due to its rolling over particle (or object) j. The rolling resistance moment can be defined by a rotational spring-dashpot model, analogous to the tangential frictional spring-dashpot model. Assuming sticking behavior, the trial rolling moment is given by

$$\boldsymbol{m}_{ij}^{rol,trial} = -k^{rol}\Delta\boldsymbol{\theta}_{ij}^{trial} - d^{rol}\boldsymbol{\omega}_{ij}, \tag{13}$$

where k^{rol} is the rotational spring stiffness, following Iwashita and Oda's [13], $\Delta\boldsymbol{\theta}_{ij}^{trial}$ is the pair's trial relative rotation, d^{rol} is the rolling damping constant and $\boldsymbol{\omega}_{ij}$ is the pair's relative angular velocity, which are given by

$$k^{rol} = 8G^*\sqrt{R^*}\delta_{ij}^{1/2}(R^*)^2, \quad d^{rol} = 2\xi^{rol}\sqrt{j^* k^{rol}}, \quad \text{and} \quad \boldsymbol{\omega}_{ij} = \boldsymbol{\omega}_i - \boldsymbol{\omega}_j. \tag{14}$$

where ξ^{rol} is the rolling damping rate, and j^* is the effective rotational inertia of the contacting pair at the contact point, given by

$$j^* = \left(\frac{1}{j_i + m_i R_i^{*2}} + \frac{1}{j_j + m_j R_j^{*2}}\right)^{-1}. \tag{15}$$

This formulation describes the conventional DEM approach . In the case of fresh concrete paste, the contact models presented in Equations eq. (2), eq. (11) and eq. (13) are replaced by a stress-based formulation derived from constitutive relations.

2.2 Discrete Fresh Concrete model

The Discrete Fresh Concrete (DFC) model, originally proposed by Cusatis and Ramyar [8], idealizes each particle as a two-phase sphere composed of a rigid inner sphere with radius r_i representing the aggregate, and an outer soft layer of thickness h representing the mortar (see Fig. 1a). The model replaces the conventional spring-dashpot contact formulation of DEM with a stress-based approach that captures the rheological behavior of fresh concrete. The motion of each particle is governed by

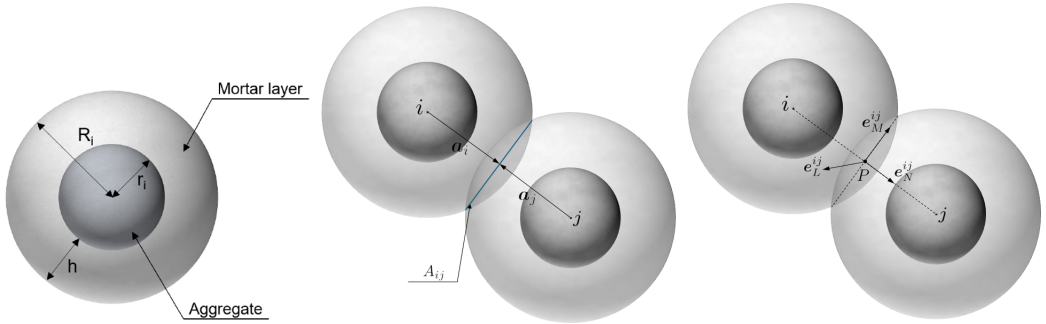
$$m_i\dot{\boldsymbol{v}}_i = \boldsymbol{f}_i^{dfc} + \boldsymbol{f}_i^{env}, \qquad j_i\dot{\boldsymbol{\omega}}_i = \boldsymbol{m}_i^{dfc}, \tag{16}$$

where $\boldsymbol{f}_i^{dfc}$ and $\boldsymbol{m}_i^{dfc}$ are contact forces and moments resulting from interaction with neighboring particles. The particle's mass m_i and rotational inertia j_i that enter in eq. (16) must now be adjusted, using an effective density to ensure that the mass of the particle system is equal to the overall mass of the material sample being represented (for details, see [9]). The contact forces and moments are given by

$$\boldsymbol{f}_i^{dfc} = \sum_{j=1}^{N_i^C} A_{ij}\boldsymbol{\sigma}_{ij}, \qquad \boldsymbol{m}_i^{dfc} = \sum_{j=1}^{N_i^C} A_{ij}(\boldsymbol{a}_i \times \boldsymbol{\sigma}_{ij}) \tag{17}$$

where $\boldsymbol{\sigma}_{ij}$ is the stress on particle i at the contact area A_{ij} with particle (or object) j and $\boldsymbol{a}_i$ is the vector from the center of particle i to the center of the contact area, as depicted in Fig. 1b. The contact area can be modeled as a circle with radius H_{ij}, which is calculated from sheer geometrical arguments as follows:

$$H_{ij} = \sqrt{(R_i)^2 - (a_i)^2} \qquad \text{and} \qquad a_i = \frac{(R_i)^2 - (R_j)^2 + (L_{ij})^2}{2L_{ij}}. \tag{18}$$



(a) (b) (c)

Figure 1. (a) DFC two-phase composite particle: rigid inner sphere representing the aggregate covered by a soft layer representing the mortar. (b) Schematics of two interacting DFC particles in a mortar-mortar contact case. (c) Local Cartesian reference system at the center of the contact area.

A local Cartesian reference system $\left\{\boldsymbol{e}_N^{ij}, \boldsymbol{e}_M^{ij}, \boldsymbol{e}_L^{ij}\right\}$ at the center of the contact area is constructed based on the normal and tangential relative velocity components, see Fig. 1c. Accordingly, $\boldsymbol{e}_N^{ij}$ is defined as the unit vector oriented along the line segment connecting the center of the two particles, calculated as follows:

$$\boldsymbol{e}_N^{ij} = \frac{\boldsymbol{x}_j - \boldsymbol{x}_i}{L_{ij}}. \tag{19}$$

Direction $\boldsymbol{e}_M^{ij}$ is then calculated from the direction of the relative tangential velocity, $\boldsymbol{v}_{rel,t}^P$, and direction $\boldsymbol{e}_L^{ij}$ is oriented as to form a right-handed coordinate system:

$$\boldsymbol{e}_M^{ij} = \frac{\boldsymbol{v}_{rel,t}^P}{||\boldsymbol{v}_{rel,t}^P||} \quad \text{and} \quad \boldsymbol{e}_L^{ij} = \boldsymbol{e}_N^{ij} \times \boldsymbol{e}_M^{ij}, \tag{20}$$

where $\boldsymbol{v}_{rel,t}^P$ is calculated from the overall relative velocity at the center of the contact area, $\boldsymbol{v}_{rel}^P$, as follows

$$\boldsymbol{v}_{rel,t}^P = \boldsymbol{v}_{rel}^P - (\boldsymbol{v}_{rel}^P \cdot \boldsymbol{e}_N^{ij})\boldsymbol{e}_N^{ij}, \quad \text{with} \quad \boldsymbol{v}_{rel}^P = \boldsymbol{v}_j + \boldsymbol{\omega}_j \times \boldsymbol{a}_j - \boldsymbol{v}_i - \boldsymbol{\omega}_i \times \boldsymbol{a}_i. \tag{21}$$

The total contact stress $\boldsymbol{\sigma}_{ij}$ is given by:

$$\boldsymbol{\sigma}_{ij} = \boldsymbol{\sigma}_s + \boldsymbol{\sigma}_v, \qquad \text{with} \qquad \boldsymbol{\sigma}_s = \begin{bmatrix} \sigma_{Ns} \\ \sigma_{Ms} \\ \sigma_{Ls} \end{bmatrix} \quad \text{and} \quad \boldsymbol{\sigma}_v = \begin{bmatrix} \sigma_{Nv} \\ \sigma_{Mv} \\ \sigma_{Lv} \end{bmatrix}. \tag{22}$$

For soft contacts (mortar-mortar and mortar-aggregate), the stress components are:

$$\boldsymbol{\sigma}_s = \begin{bmatrix} E_{Nm}\varepsilon_N^{ij} \\ 0 \\ 0 \end{bmatrix} \qquad \text{and} \qquad \boldsymbol{\sigma}_v = \begin{bmatrix} \beta\eta(\dot{\gamma})\dot{\varepsilon}_N^{ij} \\ \eta(\dot{\gamma})\dot{\varepsilon}_M^{ij} \\ \eta(\dot{\gamma})\dot{\varepsilon}_L^{ij} \end{bmatrix}, \tag{23}$$

while, for hard contacts (aggregate-aggregate), a shear stiffness term is added:

$$\boldsymbol{\sigma}_s = \begin{bmatrix} E_{Na}\varepsilon_N^{ij} \\ \alpha_a E_{Na}\varepsilon_M^{ij} \\ \alpha_a E_{Na}\varepsilon_L^{ij} \end{bmatrix} \qquad \text{and} \qquad \boldsymbol{\sigma}_v = \begin{bmatrix} \beta\eta(\dot{\gamma})\dot{\varepsilon}_N^{ij} \\ \eta(\dot{\gamma})\dot{\varepsilon}_M^{ij} \\ \eta(\dot{\gamma})\dot{\varepsilon}_L^{ij} \end{bmatrix} \tag{24}$$

where E_{Nm} is the mortar normal elasticity modulus, E_{Na} is the aggregate normal elasticity modulus, α_a is the normal-shear coupling parameter, β is a parameter that governs the viscous behavior in the normal direction,

$$\dot{\varepsilon}_N^{ij} = \frac{\boldsymbol{v}_{rel}^P \cdot \boldsymbol{e}_N^{ij}}{L_{ij}}, \qquad \dot{\varepsilon}_M^{ij} = \frac{\boldsymbol{v}_{rel}^P \cdot \boldsymbol{e}_M^{ij}}{L_{ij}} \qquad \text{and} \qquad \dot{\varepsilon}_L^{ij} = \frac{\boldsymbol{v}_{rel}^P \cdot \boldsymbol{e}_L^{ij}}{L_{ij}} \tag{25}$$

are the strain rates in the N, M and L local directions, respectively, and $\eta(\dot{\gamma})$ is the mortar's apparent viscosity, which is given by

$$\begin{aligned} \eta(\dot{\gamma}) = \eta_0 = \kappa_0\eta_\infty \quad &\text{if} \quad \dot{\gamma} \leq \dot{\gamma}_0 \\ \eta(\dot{\gamma}) = \eta_\infty|\dot{\gamma}|^{n-1} \quad &\text{if} \quad \dot{\gamma}_0 < \dot{\gamma}, \end{aligned} \tag{26}$$

where $\dot{\gamma}$ is the effective strain rate and $\dot{\gamma}_0$ is the transition strain rate, given by

$$\dot{\gamma} = \sqrt{\beta\dot{\varepsilon}_N^2 + \dot{\varepsilon}_M^2 + \dot{\varepsilon}_L^2} \qquad \text{and} \qquad \dot{\gamma}_0 = \sigma_{\tau 0}/\eta_0. \tag{27}$$

Here, $\sigma_{\tau 0}$ is the mortar shear yield stress, κ_0 is a large (penalty) constant (taken as 100, following Cusatis and Ramyar [8]), η_∞ is the mortar plastic viscosity and n refers to Newtonian ($n = 1$), shear-thickening ($n > 1$), and shear-thinning ($n < 1$) flow. When in tension, the stiffness normal stress is further compared to the mortar's tensile strength σ_t, and in case this is exceeded, σ_t is used instead (elastic-perfectly plastic static stiffness model). The mortar viscous behavior amounts to a classical regularized Bingham-Hershell-Bulkley model. In eq. (23), the absolute strain that enters the stiffness stress in the normal direction is computed by $\varepsilon_N^{ij} = ln(\frac{L_{ij}}{L_{ij0}})$.

3 Numerical Solution Scheme

The dynamical system is solved through numerical integration of the governing equations (eq. (16)) using an explicit forward Euler scheme. At each time step, the positions, velocities, angular velocities, and incremental rotations at $t + \Delta t$ are computed from their known values at time t. The time is then advanced by Δt, and the updated quantities are propagated to the next iteration. This procedure is repeated iteratively until the final simulation time t_F is attained.

The particle's velocity and the particle's spin (angular velocity) at time $t + \Delta t$ are given by:

$$\begin{aligned} \boldsymbol{v}_i(t+\Delta t) &= \boldsymbol{v}_i(t) + \frac{1}{m_i}\int_t^{t+\Delta t}(\boldsymbol{f}_i^{dfc} + \boldsymbol{f}_i^{env})dt \approx \boldsymbol{v}_i(t) + \frac{\Delta t}{m_i}[\boldsymbol{f}_i^{dfc}(t) + \boldsymbol{f}_i^{env}(t)] \\ \boldsymbol{\omega}_i(t+\Delta t) &= \boldsymbol{\omega}_i(t) + \frac{1}{j_i}\int_t^{t+\Delta t}(\boldsymbol{m}_i^{dfc})dt \approx \boldsymbol{\omega}_i(t) + \frac{\Delta t}{j_i}[\boldsymbol{m}_i^{dfc}(t)]. \end{aligned} \tag{28}$$

The position and incremental rotation at time $t + \Delta t$ are updated as follows:

$$\begin{aligned} \boldsymbol{x}_i(t+\Delta t) &= \boldsymbol{x}_i(t) + \boldsymbol{v}_i(t+\Delta t)\Delta t \\ \boldsymbol{\alpha}_i^{\Delta}(t+\Delta t) &= \boldsymbol{\omega}_i(t+\Delta t)\Delta t. \end{aligned} \tag{29}$$

The solution process is schematically outlined in the algorithm below:

Solution Algorithm

Step 1	Initialize time variables and get initial conditions:
	$t = 0$, $\Delta t =$ given, $t_F =$ given
	$\boldsymbol{x}_i(0)$, $\boldsymbol{v}_i(0)$, $\boldsymbol{\omega}_i(0)$, $\boldsymbol{\alpha}_i(0)$ = given $\quad (i = 1, \ldots, N_p)$
Step 2	**While** $\quad t \leq t_F$, loop over all particles: **For** $i = 1, \ldots, N_p$ **Do**
	Compute forces and moments at time t via eq. (17) (with eqs. eqs. (18) to (24)) and assuming that $\boldsymbol{f}_i^{env} = m_i \boldsymbol{g}$
	Update velocity, spin, position, and incremental rotation vectors:
	$\boldsymbol{v}_i(t + \Delta t) = \boldsymbol{v}_i(t) + \frac{\Delta t}{m_i}[\boldsymbol{f}_i^{dfc}(t) + \boldsymbol{f}_i^{env}(t)]$,
	$\boldsymbol{\omega}_i(t + \Delta t) = \boldsymbol{\omega}_i(t) + \frac{\Delta t}{J_i}[\boldsymbol{m}_i^{dfc}(t)]$,
	$\boldsymbol{x}_i(t + \Delta t) = \boldsymbol{x}_i(t) + \boldsymbol{v}_i(t + \Delta t)\Delta t$,
	$\boldsymbol{\alpha}_i^{\Delta}(t + \Delta t) = \boldsymbol{\omega}_i(t + \Delta t)\Delta t$
	Save updated variables:
	$\boldsymbol{v}_i(t) \leftarrow \boldsymbol{v}_i(t + \Delta t)$,
	$\boldsymbol{\omega}_i(t) \leftarrow \boldsymbol{\omega}_i(t + \Delta t)$,
	$\boldsymbol{x}_i(t) \leftarrow \boldsymbol{x}_i(t + \Delta t)$,
	$\boldsymbol{\alpha}_i(t) \leftarrow \boldsymbol{\alpha}_i(t + \Delta t)$,
	$t \leftarrow t + \Delta t$
	End do

4 Results

In this section, we present the simulation results for single-layer deposition using the proposed DEM-DFC framework. Two representative geometries were considered: a circular path and a rectangular path, both simulated under the same material and process conditions. These examples aim to evaluate the model's ability to capture filament formation and its adaptation to different deposition trajectories.

Both simulations were performed using a concrete mixture with aggregate diameters ranging from $1.5\ \mathrm{mm}$ to $3.0\ \mathrm{mm}$, following a Füller sieve curve distribution (for more details, see [9]). The cement content of $900\ \mathrm{kg/m^3}$. The water-to-cement ratio was set to 0.40, and the aggregate-to-cement ratio to 1.35. Each particle was modeled with a surrounding mortar layer of $2.75\ \mathrm{mm}$ thickness. The elastic modulus of the mortar in the normal direction was $49.0\ \mathrm{kPa}$, with a tensile strength of $5.0\ \mathrm{kPa}$. The shear yield stress of the material was $250\ \mathrm{Pa}$, and the plastic viscosity was defined as $50\ \mathrm{Pa \cdot s}$. The time step used for numerical integration was set to $\Delta t = 1.0 \times 10^{-4}\ \mathrm{s}$. The printing speed was set to $6.5\ \mathrm{cm/s}$ for the circular path and $4.0\ \mathrm{cm/s}$ for the rectangular path.

The simulation outcomes highlight the framework's ability to reproduce realistic filament behavior. The first case corresponds to a circular deposition path and was performed with a total of 6186 particles. To generate the circular trajectory of the nozzle during printing, the rotation was parameterized using the Rodrigues rotation tensor, whose main advantage is that it eliminates the trigonometric functions used in the Euler rotation vector, see Campello [14]. The second case represents a rectangular trajectory and was simulated with 3609 particles. In both cases, the extruded filament maintains its coherence and adheres to the imposed geometry (see Fig. 3).

To better represent realistic deposition conditions, different nozzle geometries were adopted for each path. For the circular path, a rectangular nozzle with a width of $28.8\ \mathrm{mm}$ and a height of $13.8\ \mathrm{mm}$ was employed, attached to a tapered tip measuring $35.5\ \mathrm{mm}$ in total height. The outlet section of the nozzle was reduced to $9.5 \times 28\ \mathrm{mm}$. For the rectangular path, a cylindrical nozzle with a diameter of $20.4\ \mathrm{mm}$ and a height of $25.0\ \mathrm{mm}$ was used. These geometries were based on typical experimental setups available in Quintana-Ruiz and Campello [10], and are illustrated in Fig. 2.

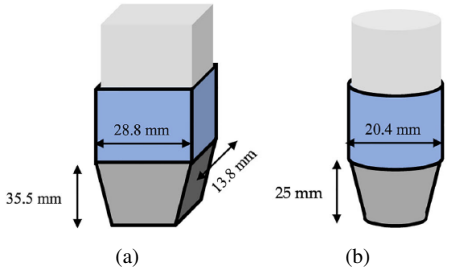
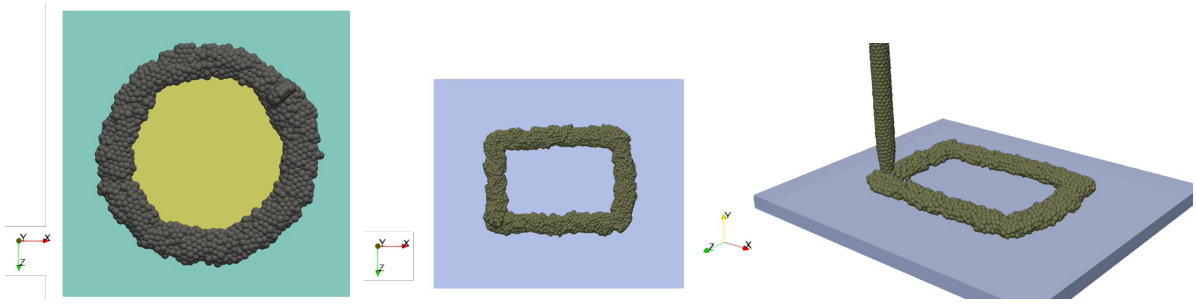


Figure 2. Nozzle geometries used for the simulations: (a) rectangular nozzle used in the circular path; (b) cylindrical nozzle used in the rectangular path.

5 Conclusions

This work presented a simulation framework for three-dimensional concrete printing based on the Discrete Element Method (DEM) combined with the Discrete Fresh Concrete (DFC) model. The framework was used



(a) (b) (c)

Figure 3. (a) Simulation along a circular trajectory. (b) Top view of a rectangular path. (c) Isometric view of the rectangular path.

to simulate single-layer extrusion over two representative deposition paths: circular and rectangular. The results demonstrate the model's capability to reproduce filament formation and stability under different geometric constraints, highlighting its potential to support the analysis of printing processes. While this study focused solely on the geometric aspects of filament deposition, the implemented framework is also capable of handling parametric studies involving material composition and process conditions. These capabilities, explored in previous works by the authors, open possibilities for supporting the optimization of 3D concrete printing through numerical simulations. Future developments may include the incorporation of additional rheological phenomena, multi-layer simulations, and experimental validation to further enhance the predictive capabilities of the model.

Acknowledgements. First author acknowledges support by CAPES (Coordenação de Aperfeiçoamento de Pessoal de Nível Superior) Brazil. The third author acknowledges support from CNPq (Conselho Nacional de Desenvolvimento Científico e Tecnológico), Brazil, under grant 313046/2021-2 and 306132/2024-9.

Authorship statement. The authors hereby confirm that they are the sole liable persons responsible for the authorship of this work, and that all material that has been herein included as part of the present paper is either the property (and authorship) of the authors, or has the permission of the owners to be included here.

References

[1] S. El-Sayegh, L. Romdhane, and S. Manjikian. A critical review of 3D printing in construction: benefits, challenges, and risks. *Archives of Civil and Mechanical Engineering*, vol. 20, n. 34, pp. 1–25. https://doi.org/10.1007/s43452-020-00038-w, 2020.

[2] Z. Zhuang, F. Xu, J. Ye, N. Hu, and L. J. Y. Weng. A comprehensive review of sustainable materials and toolpath optimization in 3D concrete printing. *Materials Sustainability*, vol. 2, 2024.

[3] R. Buswell, W. Leal de Silva, S. Jones, and J. Dirrenberger. 3D printing using concrete extrusion: A roadmap for research. *Cement and Concrete Research*, vol. 112, pp. 37–49. https://doi.org/10.1016/j.cemconres.2018.05.006, 2018.

[4] P. A. Cundall. A computer model for simulating progressive, large-scale movements in blocky rock systems. *Proc. Symp. Int. Soc. Rock Mech*, vol. , 1971.

[5] P. A. Cundall. A computer model for rock-mass behavior using interactive graphics for the input and output of geometrical data. *Report MRD-2-74. University of Minnesota (for Missouri River Division, US Army Corps of Engineers)*, vol. , 1974.

[6] P. Cundall and O. D. L. Strack. A discrete numerical model for granular assemblies. *Géotechnique*, vol. 29, n. 1, pp. 47–65, 1979.

[7] E.M.B. Campello. *Um modelo computacional para o estudo de materiais granulares*. Habilitation thesis, Escola Politécnica da Universidade de São Paulo. https://doi.org/10.11606/T.3.2016.tde-26072024-072340, 2016.

[8] G. Cusatis and E. Ramyar. Discrete Fresh Concrete Model for Simulation of Ordinary, Self-Consolidating, and Printable Concrete Flow. *Journal of Engineering Mechanics*, vol. 148, 2021.

[9] V. H. M. Avancini, O. D. Quintana-Ruiz, and E. M. B. Campello. Modeling 3D concrete printing through the combined DEM-discrete fresh concrete approach. *Computational Particle Mechanics*. (accepted for publication), 2025.

[10] O. D. Quintana-Ruiz and E. M. B. Campello. DEM modeling of advanced manufacturing technologies: from SLS to 3D concrete printing. *Archive of applied mechanics*, vol. 94, pp. 2451–2469, 2024.
[11] K. Johnson. *Contact Mechanics*. Cambridge University Press, 1985.
[12] E.M.B. Campello. A computational model for the simulation of dry granular materials. *International Journal of Non-Linear Mechanics*, vol. 106, pp. 89–107, 2018.
[13] K. Iwashita and M. Oda. Rolling Resistance at Contacts in Simulation of Shear Band Development by DEM. *Journal of Engineering Mechanics*, vol. 124, n. 3, pp. 285–292, 1998.
[14] E.M.B. Campello. A description of rotations for DEM models of particle systems. *Computational Particle Mechanics*, vol. 2, pp. 109–125. https://doi.org/10.1007/s40571-015-0041-z, 2015.